Experimental and Numerical Investigation of Controlled Flow Distortion in a Subsonic Offset Diffuser by Trapped Vorticity

Bojan Vukasinovic, Travis J. Burrows, and Ari Glezer
Woodruff School of Mechanical Engineering,
Georgia Institute of Technology, Atlanta, GA 30332-0405

Matthew T. Lakebrink and Mortaza Mani
The Boeing Company, St. Louis, MO, 63042

Abstract

Controlled concentrations of trapped vorticity within a recess in the moldline of an offset subsonic ($M < 0.7$) diffuser are explored for active suppression of flow distortions in joint experimental/numerical inveatigations. The coupling between the trapped vorticity that models inherent flow separation and the global secondary counter-rotating streamwise vortices that give rise to flow distrotions is manipulated using a spanwise array of fluidic oscillating jets that are distributed across the diffuser span just upstream of the trapped vortex. The actuation modifies the topology of critical (saddle and node) points of the trapped vortex and thereby has a profound effect on the structure of the secondary flow. It is shown that optimal interactions of the actuation with the trapped vortex can lead to full suppression of the central vortex pair and redistribute the residual vorticity along the diffuser's corners. These structural changes result in significant reduction of flow distortion by about 68% (measured by the average circumferential distortion parameter) at actuation mass flow rate that is only 0.25% of the diffuser mass flow rate.

I. Background

Future supersonic aircraft will use embedded engines to attain both aerodynamic efficiency and small spot factor with extremely compact inlet system that will have to be offset to enable efficient inlet-airframe integration schemes. The realization of these compact, offset inlet systems poses significant technical challenges in terms of flow management in the two primary system elements, namely the supersonic inlet aperture and the compact, subsonic offset diffuser. The flow within the subsonic offset diffuser is dominated by the evolution of three-dimensional, secondary structures and by possible internal flow separation which can be affected by and even become coupled to shock-induced flow unsteadiness at the inlet aperture. Overall, these complex internal flow interactions result in significant total pressure losses and flow distortion at the engine face that could be mitigated by the development and implementation of active flow-control technologies upstream of the inlet aperture and within the offset diffuser. The primary focus of the present study is the application of flow control technologies to mitigate the formation of three-dimensional vortical structures and flow separation within aggressive offset diffusers and thereby minimize losses and flow distortions leading into an engine.

The flow control approach that is considered in the present work relies on the existence of trapped vorticity in a diffuser, which would occur naturally due to the local flow separation. The objective of this approach is to utilize an active control of the trapped vorticity within the separation bubble, which in turn affects not only the flow losses and the total pressure recovery, but also the 'secondary' flows within the diffuser and thereby mitigates adverse effects of the flow distortions, along with the losses. Application and manipulation of the trapped vorticity is not new in either external or internal aerodynamics. Many interesting concepts were developed in external aerodynamics over years, predominantly motivated by a notion that an airfoil circulation can be either enhanced or reduced when vorticity becomes bound to the

surface (e.g., Saffman and Sheffield, 1977). Early work by Hurley (1959) considered improvements of low-speed characteristics of a nominally high-speed airfoil profile by introduction of a large forward flap that would trap a vortex over the leading suction side. In order to maintain a 'free-streamline' attachment over the downstream flap surface (and full confinement of the vortex), Hurley utilized steady jets over the leading Coanda surface. Another concept that relied on both upstream and downstream flaps for multiple vortex capturing to the airfoil surface without any active flow control was proposed by Kasper and published by Cox (1973), of what became known as a 'Kasper' airfoil. Rossow (1978) expanded on the application of the leading edge trapped spanwise vorticity by utilization of the end-plate suction for the vortex stabilization, and claimed improvement of the resulting lift coefficients of up to 10. More relevant to the present study, several prior investigations considered utilization of trapped vorticity in diffusers, primarily motivated by reduction of the flow losses. Ringleb (1960) proposed the cusp diffuser, which is characterized by the use of a vortex-shaped cusp on a portion of the diffuser wall to reduce the boundary shear stress, creating a stationary vortex rotating in the direction of the flow. In experimental tests, it was found difficult to maintain a stable standing vortex, which was attributed to the skin friction within the cusps (Adkins, 1975 and Lee and Price, 1986). In an attempt to improve upon the cusp diffuser, a trapped vortex diffuser was developed by Heskestad (1966), and further by Adkins (1975). This design utilized an annular vortex chamber that traps lower momentum flow that would otherwise separate downstream in the diffuser. To maintain a vortex in the chamber, it was bled continuously such that flow from the diffuser constantly energizes the vortex. Designed primarily for gas turbine combustors, this approach was able to obtain a pressure recovery over 80%, with a diffuser a third of the nominal length by utilizing a 3% bleed of air flow. Subsequently, Adkins, Matharu, and Yost (1981) further refined this design to create a 'hybrid diffuser' that can provide the same benefits with a third of the bleed. In addition, it can be used with no bleed and is found to increase pressure recovery by 25% from a conventional diffuser with the same length. More recently, numerical investigations have been performed by Mariotti, Buresti, and Salvetti (2014) on the effect of altering a two-dimensional diffuser surface to include one or two contoured cavities. It was found that inclusion of these cavities can increase diffuser efficiency, along with a pressure recovery increase of 6.9% for one cavity or 9.6% for two subsequent cavities.

The physically robust, passive flow control techniques that have been successfully applied to inlet systems to improve aerodynamic interface plane (AIP) total-pressure recovery and distortion (Vakili et al. 1985, Reichert and Wendt 1996, Jirásek 2006, Owens et al. 2008) inherently lack real-time adjustability and also result in pressure losses at or near the flow boundary. In a study by Anderson and Gibb (1993), a row of vane type vortex generators in an S-duct diffuser was found to reduce distortion and increase pressure recovery at the exit plane of the inlet. The reduction of the distortion induced by the ingestion of a thick boundary layer by using vane arrays was investigated by Anabtawi et al. (1999). More recently, Anderson et al. (2002) have demonstrated in a numerical study the control effectiveness of passive, vane type vortex generators, whose characteristic cross stream scale was a fraction of the boundary layer height, to reduce losses. In a later numerical investigation, Anderson et al. (2004) showed that small-scale ("micro") vanes can be used to reduce pressure distortion at the exit plane of compact offset diffusers. Experimental work by Jirásek (2006) on complex D-throat, heavily offset inlets further corroborated the efficacy of sub-boundary layer vane actuators. Tournier and Paduano (2005) used two rows of vane type vortex generators to produce arrays of single-sense streamwise vortices in an offset diffuser at $M = 0.6$ with deliberately-imposed inlet distortions, and reported marked improvements in pressure distortion at the exit plane. Owens et al. (2008) used a single row of vortex generators in an S-duct diffuser operating in a free stream at $M = 0.85$ resulting in a reduction of the circumferential distortion levels at the engine face. Sub-boundary layer passive flow control devices (micro-ramps) for controlling shock wave boundary layer interactions were investigated via experimentally-validated numerical computations in a supersonic inlet (Anderson et al. 2006). These authors reported that these vortex generators significantly reduced the interactions and their unsteady effects on the outer flow field. Micro-ramps similar to those used by Anderson et al. (2006) were also investigated experimentally (Babinsky et al. 2009) and showed performance gains in terms of reduced shock-induced separation.

Active flow control approaches that rely on distributions of normal and skewed jets emanating from the inner surfaces of the inlet duct can lead to significant improvement in the performance of offset diffusers, with potential for rapid actuation and little or no drag penalty in the absence of actuation. Application of active flow control affords optimization and in-flight performance control both in the absence (Weigl et al. 1997, Scribben et al. 2006, Anderson et al. 2004) and presence (Vaccaro et al. 2008, Rabe 2003) of flow separation. Amitay et al. (2002) demonstrated active flow control of localized separation in internal flows in a two-dimensional S-duct using a synthetic jet control. Anderson et al. (2004) preformed a DOE analysis to optimize the use of skewed jets with significant improvements in pressure recovery and engine face distortion. Scribben et al. (2006) used vortex generator jets in a complex offset diffuser and showed drastic improvements in distortion levels and a small reduction in drag. In similar experiments, Owens et al. (2008) used various arrays of vortex generator jets in a S-duct diffuser at $M = 0.85$ to gain insight into optimal design. More recently, Gissen et al. (2009) developed different configurations of synthetic jet arrays that generated fluidic counterparts to passive sub-boundary layer control devices in high subsonic flow in a 2D equivalent of an offset diffuser.

More recently, a hybrid control approach, which incorporates the advantages of both passive and active control, has been shown to be effective in the reduction of parasitic drag while maintaining fail-safe attributes and satisfying the need for adjustable flow control (Owens et al. 2008, Anderson et al. 2009). Owens et al. (2008) combined active and passive flow control using micro-vanes and -jets to improve the performance of an offset diffuser over a range of flow rates, especially at low velocities for which the micro-vanes were not optimized. In an effort to reduce engine bleed, Anderson et al. (2009) combined the micro-ramps used in their earlier work (2006) with flow injection resulting in an almost 10-fold reduction in required engine bleed. Vane type vortex generators have been extensively studied as a means for controlling separation in adverse pressure gradients (Godard and Stanislas 2006), as well as for use in s-ducts (Anabtawi et al. 1999, Anderson et al. 2004, Tournier and Paduano 2005) and as the passive component of hybrid flow control systems (Owens et al. 2008, Dagget et al. 2003). Nonlinear superposition of active and passive devices to create a fail-safe adjustable hybrid flow control device can be highly-effective performance enhancers for embedded propulsion systems with minimal system-level penalties in terms of weight, power consumption, robustness and maintenance.

Delot, Garnier, and Pagan (2011) experimentally evaluated the effectiveness of passive flow control with vortex generators as well as active flow control with continuous and pulsed micro-jets on reducing the AIP (aerodynamic interface plane) flow distortion in a subsonic offset diffuser, and reported a reduction by 50% at $M = 0.2$ and up to 20% at $M = 0.4$. Harrison et al. (2013) simulated and experimentally verified the effect of various blowing and suction flow control schemes on a thick boundary layer ingesting serpentine diffuser using swirl and circumferential flow distortion analysis. It is found that when using a circumferential blowing scheme, a 50% reduction of total pressure distortion can be realized. In addition, they also noted that a combination of blowing and suction can produce even higher reductions in distortion, up to 75%. Gissen et al. (2014) used hybrid flow control in an offset diffuser and showed reductions in AIP distortion levels under both active and hybrid control. They also indicated that the governing mechanism behind active redistribution of low momentum fluid in the diffuser is in the dynamics of a large-scale counter-rotating pair of vortices that are formed after a merger of the array of small-scale vortices imposed by the flow control. Gartner and Amitay (2014) studied the effect of introducing a honeycomb mesh upstream of an offset rectangular duct, and showed that the use of a honeycomb mesh can improve the symmetry of the pressure distribution while minimally decreasing the pressure recovery by pushing the saddle-saddle point of the flow that causes the onset of an instability responsible for the asymmetry of the flow, further downstream. Gartner and Amitay (2015) experimentally tested the effect of sweeping, pulsed, and two-dimensional jet actuators on the pressure recovery of a rectangular diffuser under transonic flow conditions, and showed that the sweeping jets produced higher pressure recovery at comparable mass flow rates.

A joint experimental and computational investigation at Georgia Tech and the Boeing Company focuses on the application of novel flow control technologies to minimize losses and flow distortions in

aggressive offset diffusers for improved engine operability, cruise efficiency, and maneuverability of next-generation supersonic aircraft. The inherent flow distortion and losses are mitigated by coupled, controlled suppression of the formation and evolution of internal flow separation and of naturally-occurring secondary three-dimensional vortical structures using hybrid actuation based on fluidically-controlled concentrations of trapped vorticity within the internally-separated flow. In particular, prior findings of Burrows et al. (2016) of feasibility of the present flow control approach are further optimized and the coupled experimental/CFD analysis aims at uncovering the underlying flow physics that enables the flow control effectiveness.

II. Experimental and Numerical Setup and Techniques

The experiments are performed in an open-return, pull-down, high-speed subsonic wind tunnel. The tunnel is driven by a 150 HP blower, where the temperature of the return air is controlled using a chiller, coupled with an ultra low pressure drop heat exchanger. Instead of the tunnel test section, the offset diffuser model is installed such that it couples upstream to the tunnel inlet contraction, and having the oncoming Mach number flow up to $M \approx 0.75$. The diffuser installed in the wind tunnel is shown in Figure 1a, while its basic geometry is defined in Figures 1b and c. It has a D-shaped throat of $H = 0.7 \cdot D$ in height, and a round, aerodynamic interface plane (AIP) with a diameter, $D = D_{AIP} = 12.7$ cm, while the offset between the throat and AIP is $1 \cdot D_{AIP}$.

The main flow diagnostic equipment integrated into the diffuser includes a standard total pressure rake to measure the flow distortion at the AIP, according to the industry standard ARP1420b (SAE, 2002), having a total of 40 probes in eight, equiangularly spaced rakes around the circumference of the AIP. The AIP total pressure rake is supplemented with a matching ring of eight static pressure ports along the diffuser wall, at the base of each rake leg. In addition, twelve and five static pressure ports are distributed along the bottom and top side of the diffuser wall, respectively. Static and total pressures are measured using a dedicated PSI Netscanner system. Each set of pressure measurements is based on sixty four independent samples, while the mean static and total pressures are based on one hundred data sets. Consequently, uncertainty in the mean pressures is estimated to be less than 1%. Also, a derived $DPCP_{avg}$ distortion parameter is estimated to have uncertainty of less than 2%. Calibration of the offset duct facility was performed relative to the reference static pressure port upstream from the duct inlet and the corresponding flow Mach number is based on the mean rake total pressure and the mean matching wall static pressure. In addition to the static and total pressure measurements, duct surface oil-flow visualization and localized visualization of the 'near field' across the control surface are utilized to elucidate the wall flow topology and assist in analysis of the vortical composition of the flow.

The computational domain used for CFD analysis, shown in Figure 2, incorporates key components of the wind tunnel at the Georgia Tech, including the contraction, fluidic oscillators, and AIP-instrumentation housing. An unstructured surface grid consisting of triangular elements is created using the Modular Aerodynamic Design Computational Analysis Process (MADCAP). A volumetric grid comprising prisms, pyramids, and tetrahedra is then constructed using the Advancing Front Local Reconnection (AFLR) software. A grid-resolution study is performed to minimize numerical error, and the resulting element

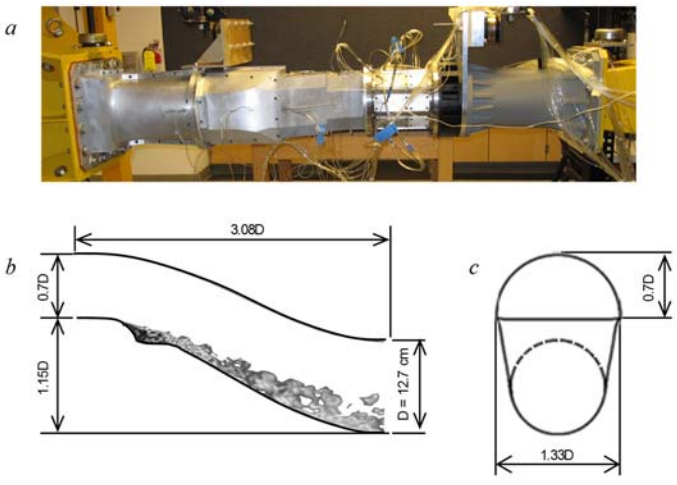

Figure 1. *Subsonic-inlet offset diffuser model integrated in the wind tunnel (a), and side (b) and downstream (c) views of its geometry with illustration of the flow over the trapped vortex (b).*

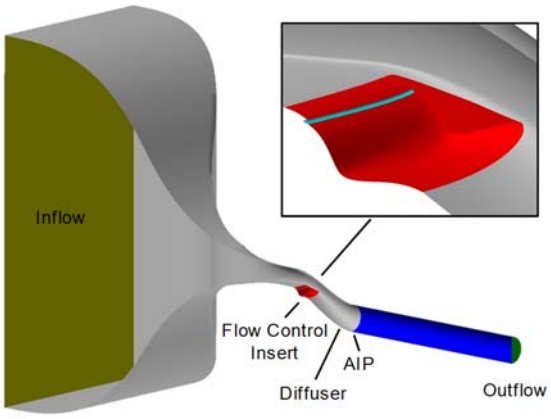

Figure 2. *Layout of the computational domain with the symmetry boundary omitted for clarity. Inset plot emphasizes the flow control insert and the jet array.*

sizes are given in Table 1 for several locations. Anisotropic triangular prisms were used to resolve the boundary layer. An initial normal spacing of 0.0001 inches was held constant for three layers away from the boundary. The growth rate for the normal spacing grew from 1.05 at layer four, to a maximum value of 1.10. Background Cartesian grids were used to enforce the size of tetrahedral elements outside of the prism layer, and the final mesh consisted of about 180-million elements.

Table 1. *Size of surface-mesh elements at several locations in the computational domain.*

Mesh Location	Element Size [in]
Diffuser Upper Surface	0.10
Diffuser Lower Surface	0.04
Flow-Control Insert	0.01
Fluidic-Oscillator Exit	0.0015

Second-order-accurate solutions to the compressible Navier-Stokes equations were obtained using the Boeing Computational Fluid Dynamic (BCFD) finite-volume flow solver. BCFD supports continuum-gas simulations of general-geometry structured and unstructured grids, for flows ranging from low subsonic to hypersonic. An extensive array of boundary conditions, numerical schemes, turbulence models, and gas models are available within BCFD for both steady-state and time-accurate simulations. In steady-state simulations, first-order implicit time integration is performed, and local eigenvalues are used to obtain a spatially varying time-step and accelerate convergence. For time-accurate simulations, a dual-time approach is used to obtain second-order temporal accuracy.

The simulations conducted for the present study assumed calorically perfect air with constant laminar and turbulent Prandtl numbers of 0.72 and 0.90, respectively. Viscosity was computed using Sutherland's law. Solid boundaries were modeled as no-slip adiabatic walls, total pressure and total temperature were prescribed on the inflow boundary, and a uniform pressure was prescribed on the outflow boundary to achieve the desired flow rate. Delayed detached eddy simulations (DDES) were conducted using Spalart-Allmaras with rotation correction and the quadratic constitutive relation (SA-RC-QCR). Bounded central differencing was employed to reduce numerical dissipation in the unsteady region downstream of the insert. The simulated flow conditions are given in Table 2. For the case with jets activated, the plenum total pressure and total temperature were held constant at 21.7 psi and 525.9 R, respectively.

Table 2. *Simulated flow conditions*

Pt [psi]	Tt [R]	P_{DS} [psi]	W_{AIP} [lb/s]
14.29	525.9	11.69	5.4

The upstream portion of the diffuser's lower surface incorporates a large, removable flow control insert, spanning -0.5" < x < 5.5" that is designed to accept a variety of flow control devices. In order to mimic recirculating bubble due to a natural local flow separation in an aggressive diffuser, a passive modification of the upstream diffuser moldline is made, as already schematically shown in Figure 1b, where the recessed moldline smoothly mates with both the upstream and downstream diffuser surfaces. This passive geometry modification is made within the same removable flow control module, and can be considered a passive flow control component relative to the unaltered offset diffuser. The effect of such a diffuser modification is also illustrated in Figure 1b, which emphasizes regions of the reduced flow momentum. It should be noted, as already shown by Burrows et al. (2016), that the flow in this diffuser has minimal distortion at the AIP, with a thin incoming boundary layer, in the absence of the recessed moldline modification. Such a thin incoming vorticity layer evolves into a rather weak and confined secondary flow along the diffuser's path, which results in nearly negligible total pressure distortion at the AIP. This is shown by the total pressure contour plot in Figure 3a, where the average distortion parameter

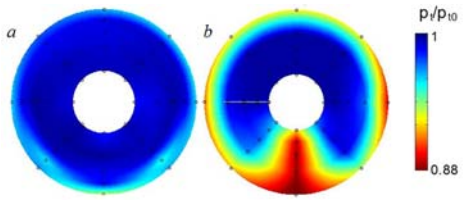

Figure 3. *Contour plot of the measured total pressure p_t/p_{to} for the smooth diffuser (a), and with the embedded trapped vortex (b).*

Figure 4. *Top view of iso-surface of helicity for the base flow. Inactive flow control jets are marked by gray arrows.*

$DPCP_{avg}$ is only about 0.008. Its counterpart for the recessed diffuser moldline is shown in Figure 3b, where the total pressure contour indicates significant total pressure deficit predominantly focused about the central lower domain. Burrows et al. (2016) noted that the total pressure pattern of the base flow (equivalent to this in Figure 3b) would match the pattern induced by a counter-rotating pair of streamwise vortices. Indeed, the present time-resolved numerical simulations clearly indicate formation of a pair of the streamwise vortices, which are shown in Figure 4 in terms of iso-surfaces of helicity. A pair of counter-rotating vortices is clearly indicated in the central zone of the lower diffuser surface. As the streamwise velocity of the diffuser flow is positive, helicity sign corresponds to the vorticity sign. This indicates that a sense of rotation of these two vortices is such that they both move the wall flow towards the central plane and then upward, thereby scooping the low momentum fluid and distributing it upward, away from the wall. These motions are directly responsible for the total pressure deficit seen in Figure 3b. Besides the vortex pair, helicity contour also isolates corner vortices at either side of the flow field. Lastly, it should be pointed out that the streamwise switch in helicity sign is associated with the flow reattachment, as the reattachment also marks a change in the streamwise velocity sign, which alters helicity sign as well.

The active part of the utilized hybrid flow control approach consists of an array of fluidic oscillating jets that are distributed across a span of the module. The flow control jets are positioned immediately upstream of the origin of flow separation, which was determined by surface oil-flow visualization over a blank insert. Figure 5a illustrates the full array of fluidic oscillating jets that were developed by Burrows et al. (2016), showing twenty-one jets that are equally spaced 7 mm apart along the span of the control insert. The present test configurations involve subsets of this full array of fluidic oscillating jets. Each jet orifice measures 1.5 × 2 mm in its nominal configuration, having the operating frequency between $f = 7 – 9$ kHz over a range of operation. The jets aim at direct control of the strength and structure of the trapped vorticity concentration, and thereby affecting the global flow within the diffuser.

Schematics showing how the control jet is embedded in the surface of the flow control module is shown in Figure 5b. The fluidic actuator is integrated under the surface moldline such that its orifice issues the jet close to tangential to the local surface. A single prototype of the fluidic oscillating jet is also characterized on the bench, and its operation is further illustrated in Figure 5c, which show schlieren visualization of the resulting jet, issuing in quiescent air. The fluidic oscillating jet cavity has two inlets which cause the two air jets to interact in an unstable fashion and adhere to one side of the orifice exit before switching to the opposite side. As this internal oscillation between the two end states repeats, the jets switching direction at the orifice manifests in the meandering jet evolution into the air, as clearly seen in Figure

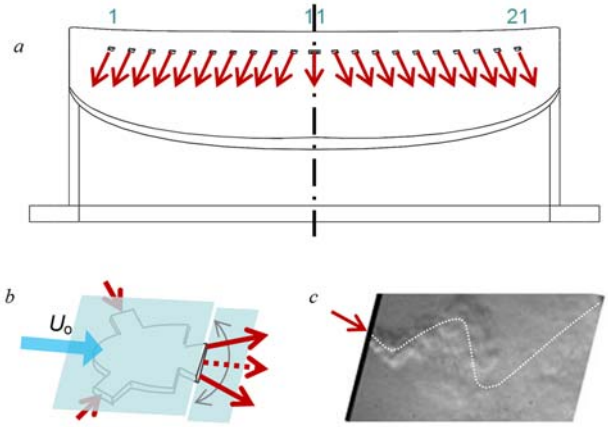

Figure 5. *Flow control module with a default configuration of 21 fluidic-oscillating jets (a), schematics of an individual fluidic oscillator integrated under the module surface (b), and schlieren visualization of the resulting jet (c).*

3c. This oscillation of the jet enhances the mixing with surrounding air and rapidly spreads the domain affected by the jet.

IV. Flow Control Effects

The investigation by Burrows et al. (2016) demonstrated that the proposed flow control alters the strength, scale, and structural topology of the trapped vorticity within the confined surface recess and consequently its interactions with the cross-flow. These controlled, indirect interactions are leveraged to significantly weaken the secondary flow within the diffuser and lead to recession of up-washed low momentum fluid, and its symmetric redistribution along the inner surfaces at the AIP. This, in turn, significantly reduces the overall flow distortion at the AIP by confining it to a thin wall layer and increasing its symmetry about the diffuser's centerline. It was shown that the effectiveness of the fluidic actuation increases with Mach number, reaching about 80% reduction in distortion at $M = 0.7$ at jet mass flow rate ratio C_q of less than 0.7%.

The present study builds on the findings of Burrows et al. (2016) and seeks further improvement of the flow control effects by tuning the interaction between the jet array and the trapped vorticity with lower jet population. Therefore, instead of utilization of the full arrays of the flow control jets, only the central subsets of the full array are utilized in the current study, aimed at controlling the centrally-formed pair of counter-rotating streamwise vortices (cf. Figure 4). This approach is first tested by examination of the effects of reducing the full control jet array from 21 to 13, and then to only seven central active jets. The corresponding contour plots of the AIP total pressure are plotted in Figure 6 with increasing jet mass flow rate coefficient C_q for $n = 21$ (Figures 6a-d), 13 (Figures 6e-h), and 7 (Figures 6i-l). Regardless of the number of active jets, there is a similar trend in decreasing deficit of the total pressure in the central lower domain, associated with the increasing deficit along the upper wall surface for the highest C_qs. Still, there are some secondary but important differences in these three cases. For instance, 'redistribution' of the deficit from the lower central zone to the upper wall surface appears rather gradual for the full jet configuration ($n = 21$), while the lowered number of jets ($n = 13$) are capable of leveling the deficit zone at rather low C_qs (Figure 6f), which is followed by deeper recovery at the central zone, but also higher deficit along the upper wall surface, with further increase in C_q (e.g., Figure 6h). It appears that the smallest array (n = 7) does not execute as effective suppression of distortion at low C_q, while at the highest, it induces induce further enhancement of both positive and negative effects in the central zone and along the side wall, respectively (e.g., Figure 6l).

Three jet configurations discussed in Figure 6 are further characterized by evolution of the main distortion parameter at the AIP, $DPCP_{avg}$ with C_q, as well as their effect on the Mach number of the diffuser flow. These results are shown in Figure 7a for $n = 21$, 13, and 7 central active jets. Changes in Mach number are utilized for assessment of the flow control effect on overall flow losses, as a decrease in Mach number indicate increased losses. Data shown in Figure 7a show that the array with fewest jets begins to introduce losses at the lowest C_q, while the Mach number of other two doesn't decrease until a slightly higher C_q. Furthermore, there is a clear trend that the rate of a decrease of M with C_q increases with a decrease in n. These drop-off levels of C_q at which M begins to decrease represent an upper

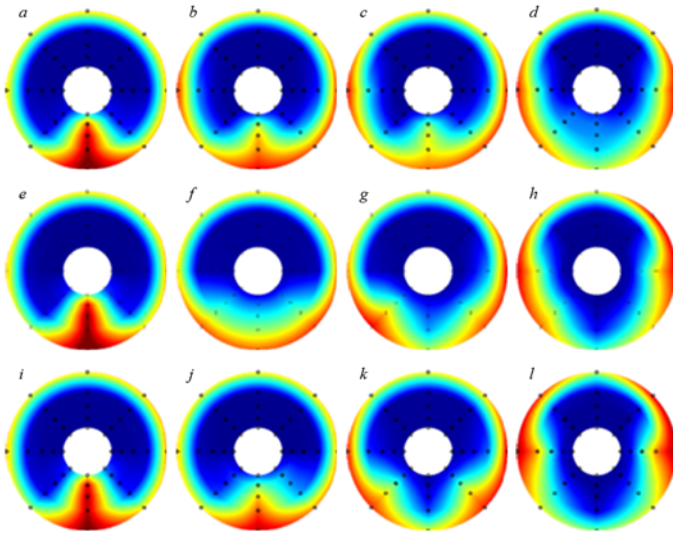

Figure 6. *Contour plot of the total pressure p_t/p_{to} for the flow controlled by n = 21 (a – d), 13 (e – h), and 7 (i – l) central jets at M = 0.7 by C_q = 0 (e,i), 0.008 (a,j), 0.0015 (k), 0.0023 (f), 0.03 (b,g), 0.038 (c,l), 0.063 (h), and 0.07 (d).*

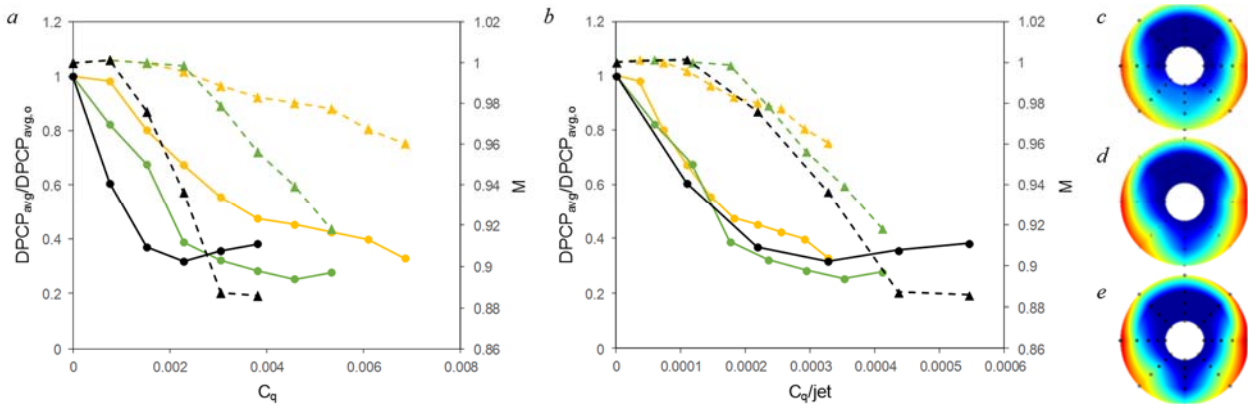

Figure 7. *Average circumferetial distortion $DPCP_{avg}$ (solid) and Mach number (dashed) with C_q (a) and C_q/jet (b) for n = 21 (yellow), 13 (green), and 7 (black), and the three contour plots of the total pressure $p_t/p_{t,o}$ for C_q/jet ≈ 3×10^{-4} and n = 21 (c) , 13 (d), and 7 (e).*

bound for a subset of the flow control rates that could be considered optimal. As for the decrease in the distortion parameter $DPCP_{avg}$ with C_q, another clear trend is shown in which the rate of $DPCP_{avg}$ decrease is inversely proportional to the number of control jets. In each of the three cases, a minimum distortion parameter $DPCP_{avg}$ is reached at about $DPCP_{avg}$ = 0.01. Although consideration of just the distortion would indicate the array with fewest jet as optimal, inclusion of the changes in Mach number shifts the best performing jet array to n = 13, as its decrease in $DPCP_{avg}$ while M is still invariant is $DPCP_{avg}$ = 0.015, due to the prolonged delay in Mach number drop for this case. Since the number of active jets is different for each of the tested cases, Figure 7b examines both $DPCP_{avg}$ and M dependence on C_q per active jet, rather than total C_q. Clearly, a unified dependence of $DPCP_{avg}$ is obtained relative to C_q/jet, which indicates that it is possible to reduce the total C_q while maintaining the same distortion reduction. Again, although this part of the analysis would point to n = 7 as the best configuration, analysis of its companion dependence of Mach number on C_q/jet shows M-invariance for the highest C_q for n = 13, again indicating this case as the most effective one from the standpoint of both recovery and distortion. Lastly, three contour plots of the AIP total pressure are plotted in Figures 7c–e for the cases when C_q/jet is approximately the same for n = 7, 13, and 21, and as it can be expected, all of these arrays effect about the same distortion changes in the diffuser flow.

Given the analysis based on the changes in $DPCP_{avg}$ and M with flow control, a summary of the flow control effectiveness in suppression of the characteristic averaged distortion parameter $DPCP_{avg}$ in shown in Figure 8 for all of the eight subset jet configurations for M_o = 0.7. As the number of jet varies and the actuation mass flow rate increases, the set Mach number in the facility M_o can vary somewhat as a result of the interactions of the jet array with the cross flow. Figure 8 therefore shows the variation of $DPCP_{avg}$ in the presence of actuation with the normalized increment of the set Mach number $\Delta M/M_o$ (M_o = 0.7) for different jet subsets. Again, there is a clear unified trend for all the data and the varying number of jets n. Initially, there is a sharp decrease in distortion, associated with weakly positive or neutral effect on Mach number, as the jets total C_q begins to increase from zero. As the near-saturation level is reached, the control jets also reach their maximum effectiveness, and further increase in the control C_q

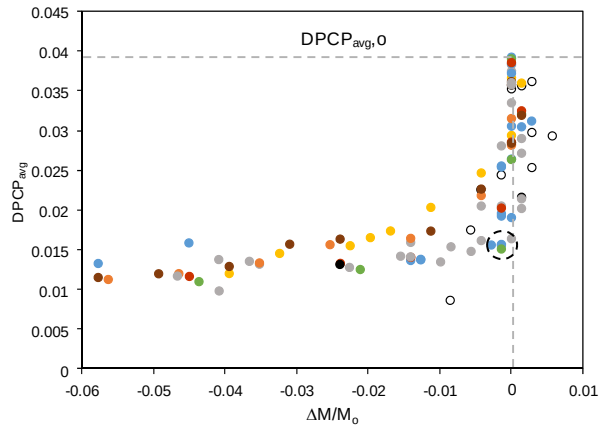

Figure 8. *Total pressure distortion parameter $DPCP_{avg}$ with Mach number for the controlled flow at M = 0.7 by n = 21 (●), 19 (●), 17 (●), 15 (●), 13 (●), 11 (●), 9 (●), and 7 (●) active jets.*

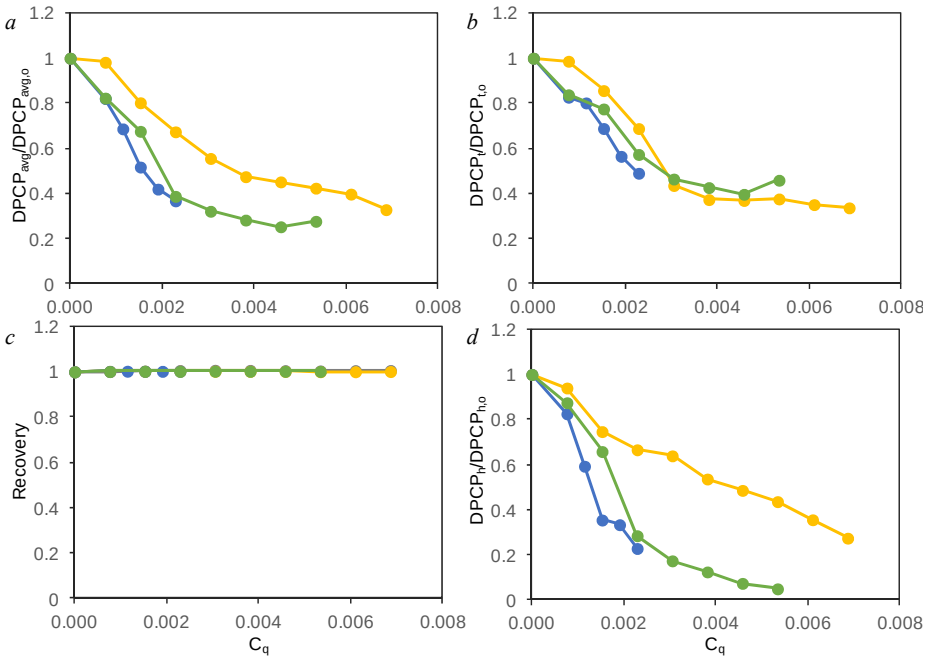

Figure 9. *Total pressure distortion parameter $DPCP_{avg}$ (a), $DPCP_t$ (b), and $DPCP_h$ (d) and recovery (c) at M = 0.7 and with the control parameter C_q for the flow control configurations with n = 21 (●), 13 (●), and 11 (●) active jets.*

is mostly converted into increased losses, manifested in a decrease in M. These compound data further show that a reduction of about two-thirds in the distortion of the base flow ($DPCP_{avg,o}$) can be attained with about half the number of active jets of the full array, at almost a third of the actuation flow rate (compared to the full array control) and negligible change in Mach number $\Delta M/M_o$ = -0.2%. Based on the aforementioned criteria, the two most effective arrays can be isolated as n = 11 and 13, among all the eight tested array configurations.

Further insight into the effectiveness of n = 11 and 13 configurations is gained by examination of a broader range of the distortion parameters and recovery of the diffuser flow. A subset of this comparison is shown in Figure 9, where evolutions of the three distortion parameters ($DPCP_{avg}$, $DPCP_h$ and $DPCP_t$) and recovery with C_q are shown for the two best cases (n = 11 and 13), and the full array for reference. These data show that the actuation significantly reduces all the three circumferential distortion measures. Perhaps the most striking feature of the changes effected by the reducing number of jets in the array is that it significantly enhances the receptivity of the base flow to the actuation. Therefore, actuation with the reduced number of jets leads to a sharp suppression in all distortion parameters, even at the lowest levels of C_q compared to the full actuation array. More importantly, however, is the demonstration that the most effective flow control configuration (n = 13) that yields a reduction in $DPCP_{avg}$ of nearly 68%, utilizes nearly half the number of active jets and almost a third of the actuation flow rate (C_q down from about 0.7% for the full array to about 0.25% for n = 13). This study clearly indicates that there is no sharp cutoff in the optimal performance of the flow control subarrays, while still pointing out that, among the tested cases, n = 13 can be

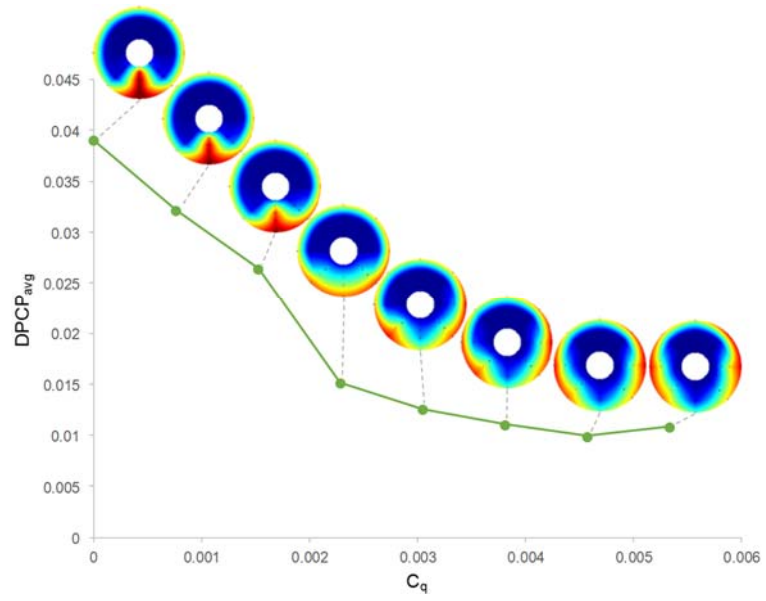

Figure 10. *Average circumferetial distortion $DPCP_{avg}$ and the corresponding contour plots of the total pressure with C_q for the optimal n = 13 jets configuration.*

selected as the best candidate for the flow control optimized effectiveness. Furthermore, the present study also indicates that more effective actuation configurations can be sought and optimized in both n and C_q, as a balance between n and C_q is shown to be the most critical for optimized performance. It is believed that the present findings also have broader implications on optimization of the flow control effectiveness, in particular in internal flows where both flow distortions and losses need to be considered simultaneously for evaluation of the flow control effectiveness.

A more detailed look at the AIP total pressure distortion for the selected flow control configuration (n = 13) is shown in Figure 10. Initially, averaged circumferential distortion parameter $DPCP_{avg}$ rather steadily decreases with C_q, as the lower central zone of the reduced total pressure becomes pushed towards the wall and up, in a thin wall layer. This trend breaks down at the point when the initial focused distortion becomes completely spread in a bottom layer at $C_q = 0.0023$. Past that point, further increase in C_q continues to increase total pressure about the central zone, but it also pushes the two halves of the low momentum fluid further up, along the walls. As these two effects oppose each other, with respect to the flow distortion, their net effect on the further reduction of distortion becomes negligible. This is a reason that the optimum C_q for this flow configuration is attained at about $C_q = 0.0023$.

CFD simulations of the diffuser flow under the optimal flow control (n = 13, C_q = 0.25%) and for the base flow (in absence of the flow control), are utilized to understand the underlying changes in the flow dynamics that result in the aforementioned favorable reduction in the flow distortions. First, Figure 11 examines instantaneous flow structure about and immediately downstream of the flow control source, which is located at the upstream section of the surface depression, without (Figures 11a and b) and with (Figures 11c and d) flow control. Flow separation over the depressed surface, from the centerline to the sidewall, is depicted in Figure 11 using an iso-surface of q-criteria colored by Mach number at a representative instant in time. In all the plots, only one half of the flow field is shown due to symmetry. Figures 11a and c are shown in isometric views, oriented from the centerline to the sidewall, having the flow from upper left to lower right, while Figures 11b and d are top-down views with flow from left to right. In either case, the flow control jet orifices are visible in the upstream row, particularly in the top views. Note that all twenty one actuators are embedded in the surface, but only the central thirteen of them are active during the flow control activation. For the base flow (Figures 11a and b), as the main flow separates off the leading edge of the surface depression, resulting shear layer evolves into the pockets of identifiable large-scale turbulent eddies, which appear fairly uniformly distributed across the diffuser span. Underneath the shear layer, separated flow forms a slowly-rotating recirculaing bubble (in the mean sense), which is fairly featureless in the instantaneous view. There are several important features of the instantaneous controlled flow, as depicted in Figures 11c and d. First, as the flow control is activated through the central jets, all of the active jet orifices indicate intense small-scale vortical motions being issued into the bulk flow. As a result, lower left side of the flow in Figure 11c and bottom portion of the flow in Figure 11d exhibit trains of small scale eddies that appear to quickly interact and presumably disrupt large-scale eddy formation and dynamics through their enhanced mixing, production and dissipation of turbulent kinetic energy

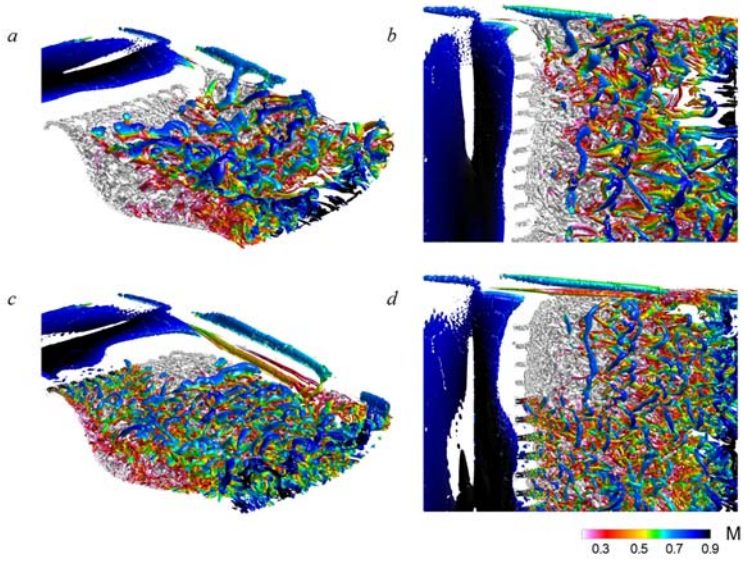

Figure 11. *Simulated baseline (a,b) and controlled (d,e) flow iso-surfaces of Q-criterion colored by Mach number for M = 0.7 and C_q = 0.25%.*

(Vukasinovic, Rusak, and Glezer, 2010). This region of the flow immediately downstream from the flow control sources appears to be almost divided into two regions: a central that is affected by the flow control actuation, and a side region that initially begins to evolve in a similar fashion as in the base flow, exhibiting similar flow structure of the evolving shear layer. Second important feature of the controlled flow is seen in comparison of the recirculating zones in Figures 11 a (base) and c (controlled). Although there is apparently some effect on the earlier flow reattachment on the downstream side of the bubble in the controlled flow, the initial increased mixing in the controlled shear layer spreads it immediately downward towards the lower surface, and the whole subsequent shear layer appears to be better 'aligned' with the bulk downward flow in the diffuser. Consequently, the recirculating bubble does not only become shortened due to the earlier reattachment, but also compressed towards the wall, which allows for more streamlined flow reattachment.

Assessment of the flow control effect over the surface depression is further assisted by experimental surface oil-flow visualization for elucidation of local and global flow topology within the diffuser and, in particular, downstream from the flow control jets. Oil for visualization is made out of a mixture of linseed oil and titanium-dioxide paint, where a balance between the two was determined iteratively, yielding a viscosity that matches the Mach number range and responds to the shear at the diffuser operating condition. First insight into the baseline and controlled flow topology is gained by utilizing surface oil-flow visualization over the flow control insert surface, where the oil is applied from just downstream from the jets array to the downstream end of the flow control insert. As an illustration of the flow control effect, two traces are shown in Figure 12 for the Mach number $M = 0.58$. Figure 12a indicates the baseline flow topology, which is dominated by the two reattachment domains separated by the central saddle point, each having a node close to the side wall, as marked on the image. It can be argued that the corner/end effects of the evolving D-shaped diffuser geometry induce the local corner flow reattachment at the nodes, which in turn forces the flow symmetry about the central plane through the saddle point. This reattachment dynamics also indicates highly three-dimensional flow in the separation bubble, and points to the near-wall flow directionality towards the central plane. The CFD counterpart of the base flow oil-flow visualization is also shown in Figure 12b, indicating a good

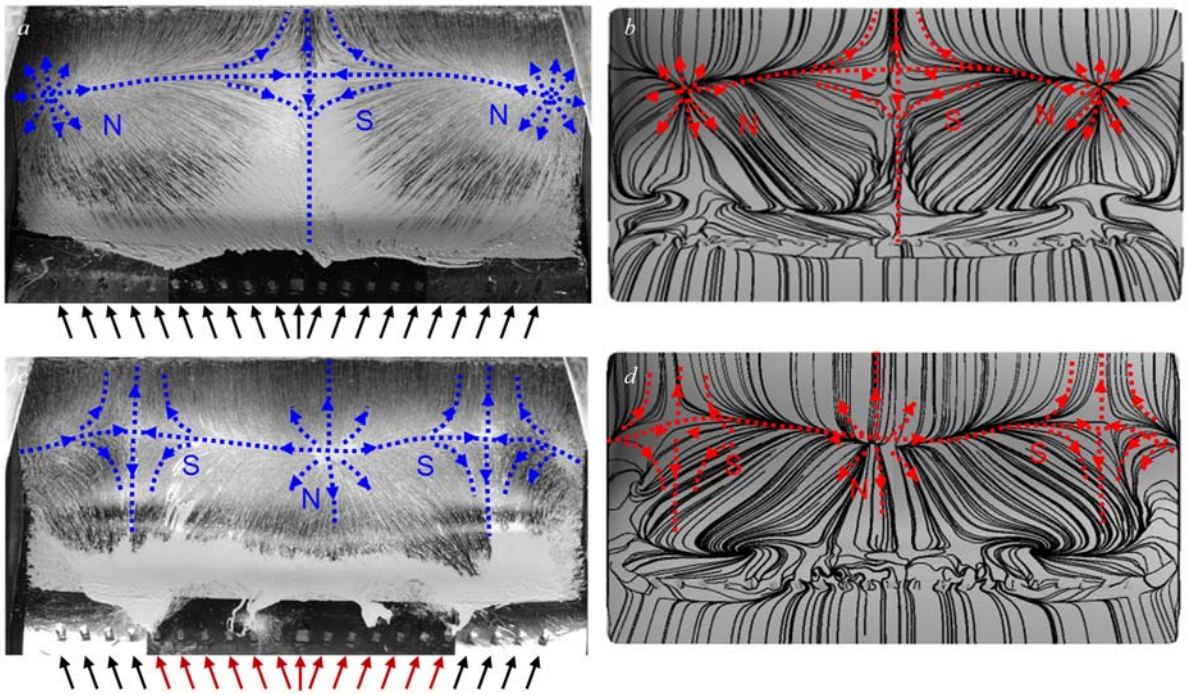

Figure 12. *Experimental (a,c) and numerical (b,d) surface oil-flow visualization over the flow control insert of the M = 0.7 baseline (a,b) and the flow controlled by the central n = 13 jets at C_q = 0.25%.*

agreement between the experimental and numerical topology of the base flow. The experimental and numerical flow topologies for the controlled (C_q = 0.25%) flow are shown in Figures 7c and d, respectively. The red arrows below Figure 12c mark the active jets for the subset of central 13 flow control elements. As it can be expected from analysis of Figure 11, the jets effect is reflected in the reduction of the reattachment length of the separated flow. However, more importantly, besides changes in the global scales of the recirculating domain, the flow topology becomes completely altered from the base flow. Besides the corner reattachment nodes, there is a central node that is formed due to the jet-forced flow attachment. Furthermore, having the two nodal streams colliding on each half of the flow creates the two saddle points that bound a large central region of the reattaching flow that occupies about 2/3 of the span. Just as the colliding streams about the central saddle point in the base flow (Figure 12a) induce a pair of streamwise vortices (cf. Figure 4) that are responsible for the large central zone of the flow distortion (cf. Figure 3b), the altered flow topology in Figure 12b suggests that such a central source of distortion would be suppressed under the flow control imposed by the central active jets.

After assessing the 'local' flow control effect immediately downstream from the flow control source, a broader look at its global effects is sought through examination of the full simulated diffuser flow fields, with (C_q = 0.25%) and without the flow control. Instantaneous and time-averaged contours of the predicted streamwise velocity on the center plane between the throat and AIP are shown in Figures 13a and c, and Figures 13b and d, respectively. Base flow is shown in Figures 13a and b, while Figures 13c and d depict the controlled flow. Past the base flow separation, a thick wall region of momentum deficit is formed in the base flow, and it persists downstream all the way to the AIP. Even as the base flow reattaches past the surface depression, the velocity deficit is created and no recovery in the base flow is facilitated prior to the AIP, and the base flow (Figure 13b) approaches the AIP with a considerable velocity deficit that extends off the wall to about 80% to the axis. As already seen in the near field of Figure 11, earlier reattachment of the separated flow under the flow control is also associated with increased vectoring of the shear layer and its 'alignment' with the flow geometry, which leads to significant suppression of the velocity deficit in the mean sense, as seen in Figure 13d. In an instantaneous sense, even with the flow control active, there are unsteady pockets of lower momentum fluid that continue to be convected along the lower diffuser wall, as it can be seen in a snapshot in Figure 13c. The flow fields in Figures 13c and d suggest that the separated flow becomes fully attached at the downstream end of the flow control insert when the diffuser flow is controlled, and that a very small residual momentum deficit gets convected into the AIP. In addition, it is also noted that there is global increase in the total velocity magnitude across the whole flow field in the controlled flow relative to the baseline.

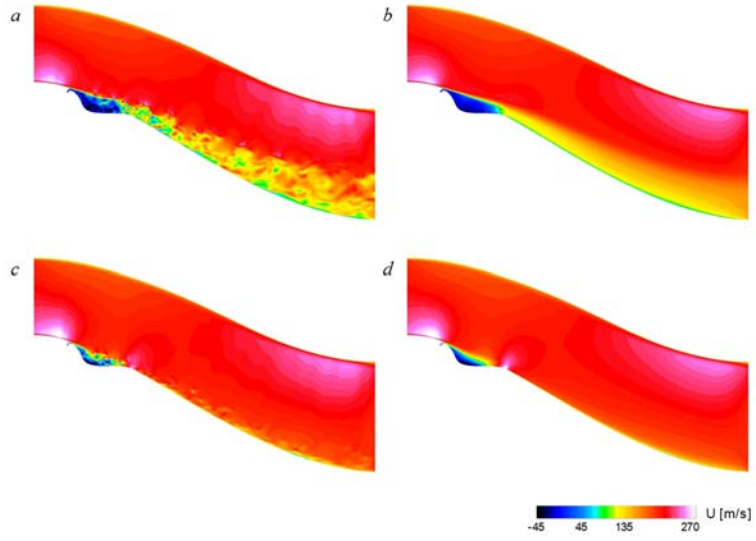

Figure 13. *Central-plane contour plots of the simulated baseline (a,b) at M = 0.7 and the flow controlled by the central n = 13 jets at C_q = 0.25% (c,d): instantaneous (a,c) and time-averaged (b,d) contour plots of the streamwise velocity component U.*

Vorticity flow fields that correspond to the flow fields shown in Figure 13 are presented in Figure 14 in terms of the iso-surfaces of instantaneous *q*-critera for vorticity detection. They are shown to differentiate instantaneous vortical compositions of the flow in the absence and presence of the flow control. The *q*-criteria plot of the base flow (Figure 14a) shows strong vorticity formation

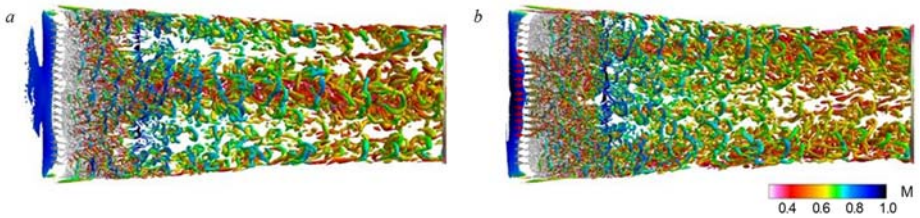

Figure 14. *Simulated baseline (a) and controlled (b) flow isosurfaces of Q-criterion vorticity for M = 0.7 and C_q = 0.25%, colored by Mach number. Active jets are marked by red arrows.*

across the full span, once the flow separates over the surface depression, which is associated with the resulting shear layer. However, once the flow reattaches, the vortex population remains dense about the centerline of the diffuser, which is attributed to the formation of the pair of counter-rotating streamwise vortices, and along the corners, due to the roll-up of the corner vortices. There is a clear separation between the two clusters of vorticity, with the central one being dominant. Although the active jets serve as vorticity sources themselves, their small-scale mixing and dissipative action on the base large-scale vortical structures act as to greatly reduce strong vortical population in the controlled flow, along the central path (Figure 14b). As already discussed in conjunction with Figure 11, there is a distinct interaction region between the flow control jets and the shear layer immediately downstream from the issuance of the central active jets (marked on the side by red arrows). Moreover, once the separated flow reattaches, the central region of the diffuser becomes nearly void of vortical structures that were dominant in the base flow. Along with suppression of the vortical structures in the central zone, the flow control appears to induce increased vorticity population on either side of the diffuser side walls (Figure 14b), which presumably originates from the two saddle points created upon the controlled flow reattachment (cf. Figure 12). Hence, the flow control effect of the vorticity field can be seen in diminishing the baseline large-scale vortices along the centerline, while introducing a distribution of smaller vortices at outboard locations, which eventually mix with the corner vortices and presumably dissipate their coherence.

In summary of the underlying flow dynamics that result in a given diffuser flow distortions for the base and controlled flows (C_q = 0.25%), Figure 15 connects the local-to-global flow topology in either flow with the resulting AIP distortion. Helicity contours are extracted from the simulations of the baseline and controlled flows. Figure 15a shows the helicity contours for the baseline, while Figure 15d shows the helicity contours for the controlled flow, a view extending from the upstream separation point to the AIP, which is represented by an oval. Numerical results of the AIP total pressure distributions are shown in Figures 15b and e, while their experimental counterparts are shown in Figures 15c and f, for the base and controlled flows. As clearly seen in the baseline flow representation (Figure 15a) there are two strong sources of streamwise vortical motions in the base flow. One, weaker, that originates along the corners and grows in the downstream direction, and two, the dominant central pair of counter-rotating vortices. They arguably originate at the point of collision of the two streams about the saddle reattachment seen in Figures 12a and b. Another

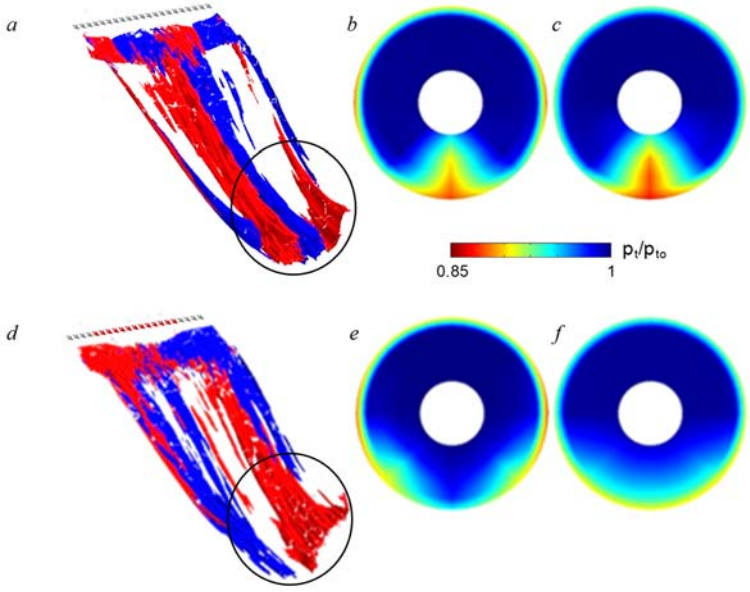

Figure 15. *Simulated baseline (a,b) and controlled (d,e) flow helicity and the AIP total pressure contours, respectively, and the experimental baseline (c) and controlled (f) AIP total pressure contour plots for M = 0.7, and n = 13 and C_q = 0.25%.*

clear connection to the local reattachment topology can be made for the controlled flow. Just as the two colliding saddle points are formed closer to the side walls under the controlled flow (see Figures 12c and d), there are two strong sources of helicity originating along these two sides in Figure 15d. Furthermore, a 'smooth' flow reattachment over the central zone, through the central node, does not give a rise to the central pair of streamwise vortices, expressed in nearly completely suppressed helicity in the central region. A clear connection between the underlying flow dynamics in the diffuser and the resulting averaged total pressure contours at the AIP can be further established. Both experimental (Figure 15c) and numerical (Figure 15b) AIP contours point to the distortion in total pressure localized about the passage of the counter-rotating vortex pair. As they move through the AIP, their sense of rotation induces a transfer of near-wall low momentum fluid towards the central plane and upward, resulting in the total pressure deficit seen in Figures 15b and c. Likewise, as these two central vortices becomes suppressed under the flow control, the central total pressure nearly recovers (Figures 15e and f). However, a rise in the streamwise vorticity along the sides (Figure 15d) also induces a small deficit along the paths of these two vortices, which is stronger pronounced in the CFD AIP contour in Figure 15e. In addition to good qualitative agreement between experimental and CFD contour plots at the AIP, this agreement can be quantified in terms of the measured recovery and average distortion measure $DPCP_{avg}$, that are 0.971 and 0.015 for the measured and 0.970 and 0.014 for the simulated controlled flows.

V. Conclusions

The performance of compact, aggressive diffusers in advanced supersonic propulsion systems is limited by internal flow separation coupled with the formation of secondary streamwise counter-roatating vortices that give rise to severe flow distortions at the engine inlet. Because the trapped vorticity concentration within the separated flow domain is susceptible to flow actuation, this interaction is leveraged for modification of the secondary flow and thereby mitigation of flow distortion. The present joint experimental-numerical investigations build on the earlier work of Burrows et al. (2016) who demonstrated the effectiveness of this hybrid flow control approach for manipulation of the coupling between trapped vorticity concentrations within an internal moldline recess of an offset diffuser and the evolution of the secondary flow vortices using a spanwise array of surface-integrated fluidic-oscillating jets. The present investigations elucidate the leverage of controlled coupling between distributions of the trapped vorticity and the secondary vortices for modifications of the total pressure distortion at the diffuser's outlet. The trapped vorticity is controlled using an upstream spanwise array of fluidic oscillating jets (operating between 7 and 9 kHz, using variable mass flow rate ratio $C_q < 1\%$). It is shown that the actuation effectiveness can be optimized by using a subset of the actuation jets in the array (eight different subsets are investigated). The investigations are conducted using a D- shape to circular diffuser ($L/D \approx 3$, $D = 12.7$ cm) having an offset of one diameter where the trapped vorticity moldline recess within the flow surface has characteristic streamwise scale of $0.7D$.

The optimal number of active actuation jets within the array is assessed using measurements of the average distortion parameter $DPCP_{avg}$ at the interface plane between the diffuser and an engine (AIP) and by the changes of the diffuser Mach number. It is found that, at least for the present setup, the reduction in $DPCP_{avg}$ saturates as C_q increases beyond a critical level. The present investigations also demonstrate that the distortion suppression is primarily dependent on the actuation C_q per jet, regardless of the number of active jets, within the limits that were tested. However, there is a lower bound on the optimal number of active jets. This is due to their adverse interaction with the cross flow that begins to incur further flow losses as the number of jets is reduced below a critical number. Consequently, there is an optimal jet array configuration that is tied to the optimal total C_q. In the present investigations, the optimal array is comprised of13 jets (out of 21 in the full array), and $C_q = 0.25\%$. The corresponding optimal flow control effectiveness is measured as an approximately 68% reduction in $DPCP_{avg}$.

The present changes in distortion are the result of suppression of the secondary streamwise vortices, which are the primary contributor to distortion at the AIP. The interaction between the trapped vorticity

and this vortex pair is characterized by a two-cell topology of the trapped vortex and the formation of a cental saddle. The sense of rotation of this secondary vortex pair is such that they transport low-momentum fluid from the diffuser surface towards the center plane, thereby creating a central domain of reduced total pressure. When flow control is applied, small-scale vorticity concentrations introduced by the actuation induce rapid mixing and spreading of the vorticity layer over the boundary of the trapped vortex. As a result of changes in entrainment, the shear layer is vectored towards the internal surface, reduces the streamwise length of the separated domain, and induces a nearly-2D attachment over the center flow domain. These changes in the topology eliminate the two-cell structure of the trapped vortex and consequently suppresses the formation of the secondary streamwise vortex pair. The elimination of the secondary vortices diminishes the distortion at the AIP. These findings indicate that coupling between a deliberately trapped vortex and the secondary streamwise vortices in the presence of separation within aggressive diffusers may be exploited for effective suppression of the distortion and losses that are associated with the 'natural' separation.

Acknowledgment

This work has been supported by ONR, monitored by Dr. Knox Millsaps.

References

Adkins, R. C. (1975). A short diffuser with low pressure loss. *Journal of Fluids Engineering*,*97*(3), 297-302.

Adkins, R. C., Matharu, D. S., & Yost, J. O. (1981). The hybrid diffuser. *Journal of Engineering for Power*, *103*(1), 229-236.

Amitay, M., Pitt, D., Glezer, A. "Separation Control in Duct Flows," *J. Aircraft*., Vol. 39, No. 4, 2002, pp. 616-620.

Anabtawi, A.J., Blackwelder, R.F., Lissaman, B.S.P, Liebeck, R.H., "An Experimental Investigation of Boundary Layer ingestion in a Diffusing S-Duct With and Without Passive Flow Control," *AIAA Paper* AIAA-99-0739, 1999.

Anderson, B., Tinapple, J., and Surber, L. "Optimal Control of Shock Wave Turbulent Boundary Layer Interactions Using Micro-Array Actuation," *AIAA Paper AIAA*-2006-3197, 2006.

Anderson, B.H., Baust, D.H., Agrell, J. "Management of Total Pressure Recovery, Distortion and High Cycle Fatigue in Compact Air Vehicle Inlets," *NASA/TM*. 2002-212000, 2002.

Anderson, B.H., Gibb, J. "Study on Vortex Generator Flow Control for the Management of Inlet Distortion," *Journal of Propulsion and Power,* Vol. 9 No. 3, 1993.

Anderson, B.H., Mace, J.L., Mani, M.,"Active "Fail Safe" Micro-Array Flow Control For Advanced Embedded Propulsion Systems," *AIAA Paper* AIAA-09-741, 2009.

Anderson, B.H., Miller, D.N., Addington, G.A., Agrell, J. "Optimal Micro-Vane Flow Control for Compact Air Vehicle Inlets," *NASA/TM*. 2004-212936, 2004.

Anderson, B.H., Miller, D.N., Addington, G.A., Agrell, J. "Optimal Micro-Jet Flow Control for Compact Air Vehicle Inlets," *NASA/TM*. 2004-212937.

Babinsky, H. Li, Y., Pitt., Ford, C.W. "Optimal Microramp Control of Supersonic Oblique Shock-Wave/Boundary-Layer Interactions," *AIAA Journal,* Vol. 47, 668-675, 2009.

Burrows, T. J., Gong, Z., Vukasinovic, B., and Glezer, A. "Investigation of Trapped Vorticity Concentrations Effected by Hybrid Actuation in an Offset Diffuser", AIAA Paper AIAA-2016-0055.

Cox, J., "The revolutionary Kasper wing," Soaring, 37, 1973, pp.20-23.

Dagget, David L. Kawai, R. Friedman, D. "Blended Wing Body Systems Studies: Boundary Layer Ingestion Inlets with Active Flow Control" *NASA/CR*. 2003-212670.

Delot, A. L., Garnier, E., and Pagan, D. "Flow control in a high-offset subsonic air intake." *AIAA Paper,* AIAA-2011-5569, 2011.

Gartner, Jeremy, and Amitay, M. "Effect of boundary layer thickness on secondary structures in a short inlet curved duct." *International Journal of Heat and Fluid Flow,* Vol. 50, pp. 467-478, 2014.

Gartner, Jeremy, and Amitay, M. "Flow Control in a Diffuser at Transonic Conditions." *AIAA Paper,* AIAA-2015-2484, 2015.

Gissen, A. N., Vukasinovic, B., and Glezer, A. "Controlled Streamwise Vorticity in Diffuser Boundary Layer using Hybrid Synthetic Jet Actuation" *AIAA Paper,* AIAA-2009-4021, 2009.

Gissen, A. N., Vukasinovic, B., McMillan, M. L., and Glezer, A., "Distortion Management in a Boundary Layer Ingestion Inlet Diffuser Using Hybrid Flow Control", *J. Propul. Power,* Vol 30, pp. 834-844, 2014.

Gissen, A. N., Vukasinovic,B., and Glezer, A. "Dynamics of flow control in an emulated boundary layer-ingesting offset diffuser" *Exp. Fluids*, Vol 50, 1794, 2014.

Godard, G. Stanislas, M. "Control of a decelerating boundary layer. Part 1: Optimization of passive vortex generators." *Aerospace Science and Technology*, Vol. 10, pp. 181-191. 2006.

Harrison, N. A., Anderson, J., Fleming, J. L., and Ng, W. F. "Active flow control of a boundary layer-ingesting serpentine inlet diffuser." *Journal of Aircraft,* Vol 50, no. 1, 262-271, 2013

Heskestad, G. (1966). Remarks on Snow Cornice Theory and Related Experiments with Sink Flows. *Journal of Basic Engineering*, *88*(2), 539-547.

Hurley, D.G., "The use of boundary-layer control to establish free stream-line flows," Advances in Aeronautical Sciences, 2, 1959, pp.662-708.

Jirásek, A., "Development and Application of Design Strategy for Design of Vortex Generator Flow Control in Inlets," *AIAA paper* AIAA-06-1050, 2006.

Lee, C. C., Price, W. A. (1986). Subsonic Diffusers for Highly Survivable Aircraft. *Air Force Wright Aeronautical Laboratories,* AFWAL-TR-86-3025.

Mariotti, A., Buresti, G., & Salvetti, M. V. (2014). Control of the turbulent flow in a plane diffuser through optimized contoured cavities. *European Journal of Mechanics-B/Fluids*, *48*, 254-265.

Owens, L.R., Allan, B.G., Gorton, S.A., "Boundary-Layer-Ingesting Inlet Flow Control," *Journal of Aircraft*, Vol. 45, No. 4, 2008.

Rabe, Angela C. "Effectiveness of a Serpentine Inlet Duct Flow Control Scheme at Design and Off-Design Simulated Flight Conditions" *PhD Thesis Virginia Tech*. 2003.

Reichert, B. A. Wendt, B. J. "Improving Curved Subsonic Diffuser Performance with Vortex Generators." *AIAA Journal*, Vol. 34, No 1, 1996.

Ringleb, F. O. (1960). Two-Dimensional Flow with Standing Vortexes in Ducts and Diffusers. *Journal of Basic Engineering*, 82(4), 921-927.

Rossow, V.J., "Lift enhancement by an externally trapped vortex," Journal of Aircraft, 15(9), 1978, pp.618-625.

Saffman, P.G. and Sheffield, J.S., "Flow over a wing with an attached free vortex," Studies in Applied Mathematics, 57(2), 1977, pp.107-117.

Scribben, A.R., Ng, W., Burdiso, R., "Effectiveness of a Serpentine Inlet Duct Flow Control Technique at Design and Off-Design Simulated Flight Conditions" *J. Turbomachinery*, Vol. 128, No. 2, pp. 332-339, 2006.

Society of Automotive Engineers Aerospace Recommended Practice 1420 Revision B, 2002-03-01

Tournier, S., Paduano, J.D."Flow Analysis and control in a Subsonic Inlet," *AIAA Paper AIAA*-05-4734, 2005.

Vaccaro, John. Vasile, J. Amitay, M. "Active Control of Inlet Ducts." *AIAA Paper* AIAA-2008-6402., 2008.

Vakili, A., Wu, J. M.., Liver, P., Bhat, M. K., "Flow Control in a Diffusing S-Duct," *AIAA Paper* AIAA-85-0524, 1985.

Vukasinovic, B., Rusak, Z. and Glezer, A., "Dissipative small-scale actuation of a turbulent shear layer," Journal of Fluid Mechanics, 656, 2010, pp.51-81.

Weigl, H. J., Paduano, J. D., Frechette, L. G., Epstein, A. H., Greitzer, E. M., Bright, M. M., & Strazisar, A. J. "Active stabilization of rotating stall and surge in a transonic single stage axial compressor." Proceedings of *ASME 1997 International Gas Turbine and Aeroengine Congress and Exhibition*, Paper 97-GT-411, 1997.